Progress Report for the SIRIUS Code Development Contract for the Period November 1, 1994 to November 1, 1995

P. Cousseau, R. Engelstad, D.L. Henderson, G.L. Kulcinski, J.J. MacFarlane, E.A. Mogahed, G.A. Moses, C. Nin, R.R. Peterson, J.F. Santarius, K. Simmons, I.N. Sviatoslavsky, P. Wang, P.P.H. Wilson

November 1995

UWFDM-996

FUSION TECHNOLOGY INSTITUTE

UNIVERSITY OF WISCONSIN

MADISON WISCONSIN

Progress Report for the SIRIUS Code Development Contract for the Period November 1, 1994 to November 1, 1995

P. Cousseau, R. Engelstad, D.L. Henderson, G.L. Kulcinski, J.J. MacFarlane, E.A. Mogahed, G.A. Moses, C. Nin, R.R. Peterson, J.F. Santarius, K. Simmons, I.N. Sviatoslavsky, P. Wang, P.P.H. Wilson

Fusion Technology Institute
University of Wisconsin
1500 Engineering Drive
Madison, WI 53706

http://fti.neep.wisc.edu

November 1995

UWFDM-996

Progress Report for the SIRIUS Code Development Contract for the Period November 1, 1994 to November 1, 1995

P. Cousseau, R. Engelstad, D.L. Henderson, G.L. Kulcinski,
J.J. MacFarlane, E.A. Mogahed, G.A. Moses, C. Nin,
R.R. Peterson, J.F. Santarius, K. Simmons,
I.N. Sviatoslavsky, P. Wang, P.P.H. Wilson

Fusion Technology Institute
Department of Nuclear Engineering and Engineering Physics
University of Wisconsin-Madison
1500 Engineering Drive
Madison, WI 53706

November 1995

UWFDM-996

U.S. Department of Energy
Contract No. DE-AS08-88DP10754

The Development and Application of
Advanced Analytical Methods to
Commercial ICF Reactor Chambers

Task 1
Progress Report

Multi-Dimensional Radiation Hydrodynamics Computer Code Development

J. F. Santarius, K. Simmons, J. J. MacFarlane,
G. A. Moses, R. R. Peterson, and P. Wang

Fusion Technology Institute
University of Wisconsin-Madison

1. Radiation Hydrodynamics Multi-Dimensional Code Development Activities in FY95

The main FY95 activities in our effort to develop a multi-dimensional radiation hydrodynamics computer code have been to

- evaluate candidate programs,
- select one code for development,
- begin modifying it, and
- run 2-D test cases.

Starting with a survey of available hydrodynamics codes, both with and without radiation, we selected three for a more extensive evaluation: CTH, MACH2, and ZEUS-2D. These were run with some simple hydrodynamics test cases and, for MACH2 and ZEUS-2D, which have a rudimentary radiation hydrodynamics (RHD) capability, some simple RHD test cases. Based on several considerations, discussed in Section 2, the ZEUS-2D code was chosen as the foundation of our 2-D radiation hydrodynamics code development effort.

Having selected a code, two types of simple but relevant ZEUS-2D test cases were run at high energy density. These cases were

1. Spherical and cylindrical explosions at high energy density, and
2. Radiation impinging on a gold slab.

These two types of cases were then merged into cases typical of actual hohlraums. The techniques learned in running the simple cases allowed us to run the hohlraum cases with reasonable time steps, although optimizing these runs remains work in progress. The results of this effort are discussed further in Section 3.

2. Radiation Hydrodynamics Code Candidates

The key considerations used in evaluating the three main candidate codes for our purposes are briefly summarized in Table 1.

The ZEUS-2D code was chosen for our development purposes because:

- ZEUS-2D already contained a simple (single frequency) radiation hydrodynamics capability, the extension of the algorithms to multiple frequencies is straightforward, and a ZEUS-3D version exists that we anticipate would expedite developing a 3-D RHD capability.
- CTH can be used for multiple materials and shock waves impacting structures, but it will be difficult to add radiation transport because it is coded with explicit numerical sweeps in alternating directions, while the radiation transport intrinsically requires an implicit solution.

Table 1. Key Considerations for the Main Codes Evaluated for Development into a Two-Dimensional Radiation Hydrodynamics Code.

	CTH	MACH2	ZEUS2D & 3D
Main applications	Projectiles; explosives	Compact toroid MHD	Astrophysics
Originator	Sandia	Phillips Laboratory	NCSA (NSF)
Restrictions	Proprietary	Proprietary	Public Domain
Language	Fortran 77 and C	Fortran 77 and C	Fortran 77 and C
Radiation diffusion	No	Yes (cooling or optically thick)	Yes (2-D)
Multi-material	Yes	Yes, in distinct regions	No
Magnetic field	No	Yes	Yes
Eulerian or Lagrangian	Eulerian (Lagrangian step and remap)	Arbitrary Lagrangian Eulerian (ALE)	Eulerian
Numerical method	Explicit	Implicit (SOR)	Explicit hydro and transport; Implicit radiation diffusion (ICCG)
Mesh	1 block	Multiple blocks	Ragged boundary
Geometry	Rectangular (3-D) Cylindrical (2-D) Spherical (1-D)	Rectangular (2-D) Cylindrical (2-D)	Rectangular (3-D) Cylindrical (2-D) Spherical (2-D)

- MACH2 contains rudimentary radiation diffusion and multi-material zones, but we judged it to be difficult to modify, and Lagrangian mesh tangling will be a serious issue for the types of 2-D calculations we need to run.

3. 2-D Radiation Hydrodynamics Code Development Status

Our earliest attempts at running hohlraum cases experienced difficulty due to the time step dropping to very small values (10^{-30} s). This appeared to be due to the coupling of the target explosion with the wall, so we investigated the simpler problems of an isolated target explosion and of the slab-geometry interaction of radiation with a gold wall. By varying the zoning, profiles, initial conditions, and background conditions, each of these problems was successfully attacked. The problems were explored up to hohlraum-relevant energy densities. That is,

- High-energy-density cases were run for cylindrical and spherical target explosions in rectangular (x,y), cylindrical (r,z), and spherical (r,θ) geometry with
  - radiation energy density $\lesssim 10^{21}$ erg/cm^3, and
  - plasma energy density $\lesssim 2.5 \times 10^{16}$ erg/cm^3.
- Blackbody radiation diffusing through a gold slab was run with
  - radiation energy density $\lesssim 2 \times 10^{11}$ erg/cm^3, and
  - plasma energy density $\lesssim 4 \times 10^{14}$ erg/cm^3.

Currently, hohlraum cases are being run, and results will be reported at the American Physical Society–Division of Plasma Physics meeting in Louisville, Kentucky, November 6–11, 1995. Preliminary cases appear qualitatively correct, but time steps are lower than desired by about a factor of 100. Optimization of the factors discussed in the previous paragraph has only begun, however, so it seems likely that efficient time steps will be achieved.

The key remaining tasks that we anticipate accomplishing for the hohlraum cases to be presented at the APS-DPP meeting are

- adding table lookup for opacities and equations of state, and
- implementing a multigroup treatment of frequency dependence.

U.S. Department of Energy
Contract No. DE-AS08-88DP10754

The Development and Application of
Advanced Analytical Methods to
Commercial ICF Reactor Chambers

Task 2
Progress Report

1-D Radiation-Hydrodynamic Modeling of Inertial Confinement Fusion High Energy Density Plasmas

J. J. MacFarlane, G. A. Moses, R. R. Peterson, and P. Wang

Fusion Technology Institute
University of Wisconsin-Madison

In this section, we describe improvements in our 1-D radiation-hydrodynamic simulation capabilities. Details of this work are provided in Reference [1].

BUCKY-1 is a one-dimensional (1-D) radiation-hydrodynamics code developed at the University of Wisconsin Fusion Technology Institute to study Inertial Confinement Fusion (ICF) high energy density plasmas. This code has been constructed in large part by integrating pieces from several other simulation codes which were developed at the University of Wisconsin to study target physics and target chamber design issues for ICF reactors. Its history is rooted primarily in the following codes:

- **PHD-IV** [2] — A 1-D radiation-hydrodynamics code written to simulate ICF target implosions, fusion burn, and energy partitioning during target breakup.
- **MF-FIRE** [3] — A 1-D radiation-hydrodynamics code for simulating the response of a target chamber buffer gas to a high-gain ICF microexplosion.
- **CONRAD** [4] — A descendant of MF-FIRE which includes the capability of simulating the vaporization of solid or liquid surfaces exposed to the x-rays and fast debris ions from high-gain targets.
- **NLTERT** [5] — A non-LTE collisional-radiative equilibrium (CRE) code with detailed radiation transport packages used to study the radiative, atomic, and spectral properties of ICF-related laboratory plasmas.

The code utilizes high-quality equation of state (EOS) and multigroup opacity tables generated by EOSOPA [6], which provides data for both low-Z and high-Z plasmas over densities ranging from the dilute ideal gas region to highly compressed matter. In addition to integrating parts of previously written codes, a number of new packages and options have been added. These include: a new multiangle, multifrequency radiation transfer model based on the method of short characteristics; an escape probability model for energy deposition of neutrons created during the DT burn phase; a simple laser energy deposition model; the ability to simulate the response of thin foil targets to an external radiation source; and more flexibility in setting up and running multilayer, multimaterial problems, including the ability to select different EOS packages (EOSOPA or SESAME) for each layer. Also it is worth noting that the output from this code has been set up to interface readily with our non-LTE spectral analysis code. This allows for an efficient means of turning temperature and density distributions predicted by BUCKY-1 into detailed emission or absorption spectra, which can then be directly compared with spectra obtained in laboratory plasma experiments.

This code and its predecessors have been used to simulate a variety of plasmas. Examples include:

- Simulation of the breakup and energy partitioning of high-gain ICF targets [7–9];
- Simulating the response of materials (Au foils, Al witness plates) to hohlraum radiation drives [10–12];

- Investigating the response of non-LTE buffer gas plasmas to ICF high-gain microexplosions [13, 14] and to laser-produced blast waves generated by fast ions [15];
- Studying the vaporization and condensation of solid and liquid surfaces exposed to ICF target x-rays and debris ions [16, 17];
- Simulation of "plastic sandwich" targets heated by intense Li beams [18, 19];
- Investigating the x-ray emission from shocks generated in the winds of high-luminosity stars [20].

At various stages of development, many of the models in the code have been tested and benchmarked. The reader should note, however, that the code is continually being modified and upgraded, and that we must continue our efforts to test the code and benchmark against experimental data whenever possible.

The major features of BUCKY-1 are as follows. It is a 1-D Lagrangian hydrodynamics code which can simulate plasmas in planar, cylindrical, or spherical geometries. It solves a single fluid equation of motion (electrons and ions are assumed to move together) with pressure contributions from electrons, ions, radiation, and fast charged particles. Shocks are handled using a von Neumann artificial viscosity. Energy transfer in the plasma can be treated using either a one-temperature ($T_i = T_e$) or two-temperature ($T_i \neq T_e$) model. Both the electrons and ions are assumed to have Maxwellian distributions defined by T_i and T_e. Thermal conduction for each species is treated using Spitzer conductivities, with the electron conduction being flux-limited. The two temperature equations are coupled by an electron-ion energy exchange term and each equation has a PdV work term.

Radiation emission and absorption terms are coupled to the electron temperature equation. Multifrequency radiation intensities are computed using a choice of several radiation transport packages: (1) a flux-limited radiation diffusion model; (2) a multiangle radiative transfer model based on the method of short characteristics (presently, planar geometry only); (3) a variable Eddington radiative transfer model (spherical geometries); and (4) a non-LTE line radiation transport package based on escape probability techniques. The sum of the contributions to emission and absorption from all frequency groups is then coupled to the electron energy equation as a source term. Multifrequency opacities are obtained from EOSOPA tables. When the CRE line transport model is invoked, non-LTE atomic level populations are computed self-consistently with the line radiation field. In this case, collisional and radiative atomic data are obtained from ATBASE [21] tables.

In addition to radiation, a number of other physical processes are included in the electron and ion energy equations as source terms: fast ion (beam or target debris) energy deposition; heating due to the deposition of fast charged particles and neutrons during the fusion burn phase; laser energy deposition; and x-ray heating of a cold buffer gas. Fusion burn equations from DT, DD, and DHe^3 reactions are solved and the charged particle reaction products are transported and slowed using a time-dependent particle tracking algorithm. Neutrons are deposited in the target using an escape probability model. Fast ions from an ion beam or target microexplosion debris are tracked using a time-, energy-, and species-dependent stopping power model. Stopping powers are computed using a Lindhard model

at low projectile energies and a Bethe model at high energies [22]. Laser energy is deposited using an inverse Bremsstrahlung attenuation model, with a dump of the remaining laser energy at the critical surface.

The source code for BUCKY-1 (without common blocks inserted) is about 27,000 lines. The code is typically run on UNIX workstations (HP 700 series, SUN, IBM RS6000, Silicon Graphics) which have 32 - 80 MB of RAM. The memory required depends on the size of the arrays, which are easily adjusted by the user. A preprocessor is used to allow for ease in adjusting array sizes and machine portability. The main functions of the preprocessor are to: insert common blocks in the source code; define array sizes through PARAMETER statements; and insert machine-dependent source code. The CPU time required for typical calculations on HP 715 and 735 workstations ranges from several minutes to several hours, depending on the complexity of the problem. Results are plotted using separate software which reads a binary output file created during the simulation.

BUCKY-1 has been benchmarked against several previously published calculations and experiments. As an example, Figure 1 compares BUCKY-1 results for the isentropic compression of a DT shell with the results of Kidder [23]. Note the trajectories of the DT zones are very similar in the 2 calculations, including the time of void closure. This and other benchmarking calculations (see Ref. [1] for additional examples) provide a means of assessing the reliability of BUCKY-1.

References

[1] MacFarlane, J.J., Moses, G.A., and Peterson, R.R., "BUCKY-1 — A 1-D Radiation-Hydrodynamics Code for Simulating Inertial Confinement Fusion High Energy Density Plasmas," University of Wisconsin Fusion Technology Institute Report UWFDM-984 (August 1995).

[2] Moses, G.A., "PHD-IV — A Plasma Hydrodynamics, Thermonuclear Burn, Radiative Transfer Computer Code," University of Wisconsin Fusion Technology Institute Report UWFDM-194 (Revised August 1985).

[3] Moses, G.A., Peterson, R.R., and McCarville, T.J., "MFFIRE - A Multifrequency Radiative Heat Transfer Hydrodynamics Code," *Computer Physics Communications* **36**, 249 (1985).

[4] Peterson, R.R., MacFarlane, J.J., and Moses, G.A., "CONRAD — A Combined Hydrodynamics–Condensation/Vaporization Computer Code," University of Wisconsin Fusion Technology Institute Report UWFDM-670 (Revised July 1988).

[5] MacFarlane, J.J., "NLTERT — A Code for Computing the Radiative Properties of Non-LTE Plasmas," University of Wisconsin Fusion Technology Institute Report UWFDM-931 (December 1993).

[6] Wang, P., "EOSOPA — A Code for Computing the Equations of State and Opacities of High Temperature Plasmas with Detailed Atomic Models," University of Wisconsin Fusion Technology Institute Report UWFDM-933 (December 1993).

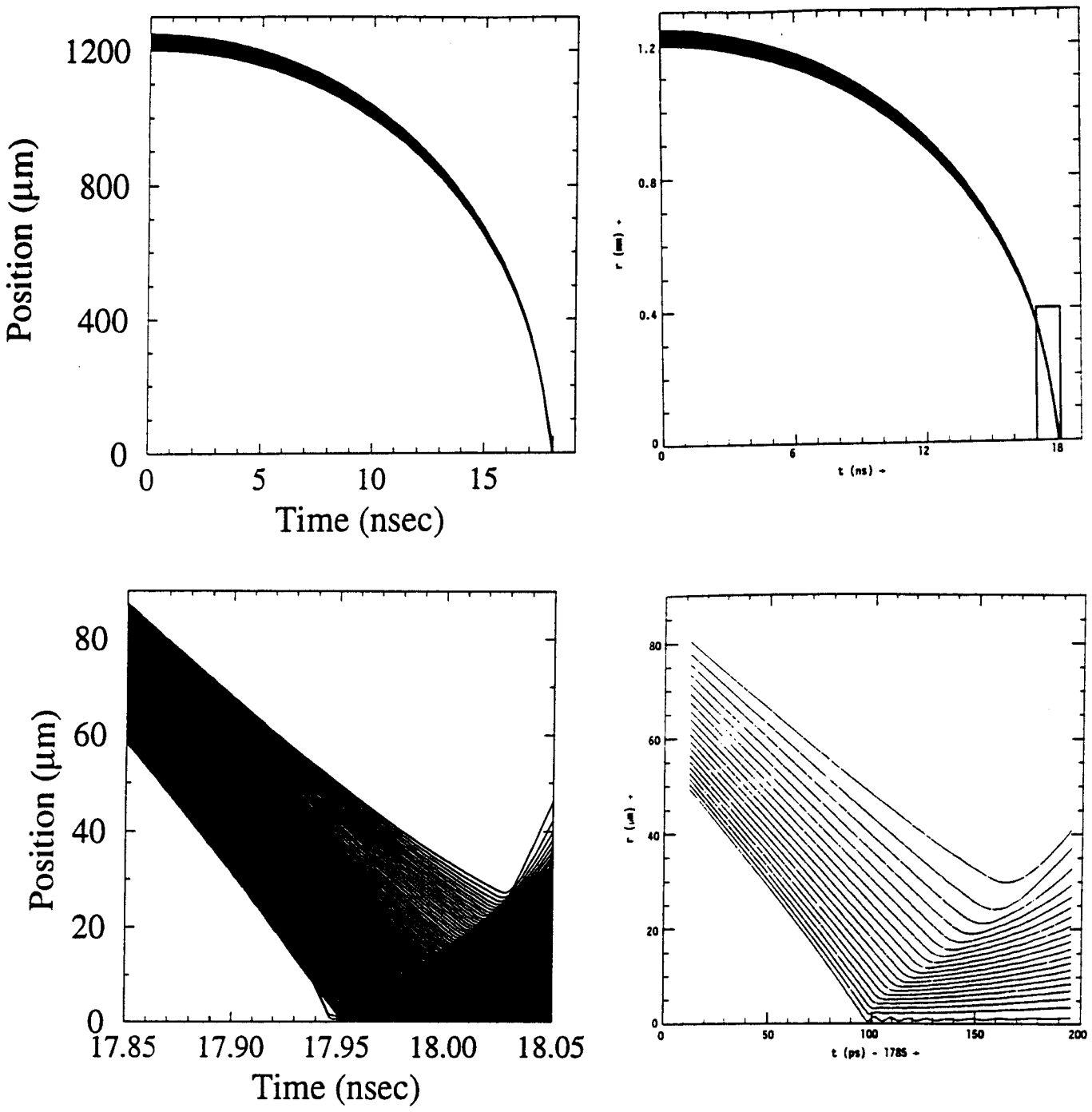

Figure 1. Lagrangian zone positons vs. time for DT isentropic compression simulation. Left: BUCKY-1 results, right: Kidder [23] results.

[7] Badger, B., et al., "HIBALL — A Conceptual Heavy Ion Beam Fusion Reactor Study," University of Wisconsin Fusion Technology Institute Report UWFDM-625 (December 1984).

[8] MacFarlane, J.J., Moses, G.A., Wang, P., Sawan, M.E., and Peterson, R.R., "Numerical Simulation of Target Microexplosion Dynamics for the LIBRA-SP Inertial Confinement Fusion Reactor," University of Wisconsin Fusion Technology Institute Report UWFDM-973 (December 1994).

[9] Peterson, R.R., Moses, G.A., MacFarlane, J.J., and Wang, P., *Fusion Technology* **26**, 780 (1994).

[10] Wang, P., MacFarlane, J.J., Moses, G.A., and Mehlhorn, T.A., "Atomic Physics Calculations in Support of Numerical Simulations of High Energy Density Plasmas," presented at the 36th Annual Meeting of the APS Division of Plasma Physics, Minneapolis, MN (November 1994).

[11] Peterson, R.R., Simmons, K., MacFarlane, J.J., Wang, P., and Moses, G.A., "Computer Simulations of the Debris and Radiation Emission from an Ignited NIF Target," presented at the 36th Annual Meeting of the APS Division of Plasma Physics, Minneapolis, MN (November 1994).

[12] MacFarlane, J.J., Wang, P., Peterson, R.R., and Moses, G.A., presentations at Lawrence Livermore National Laboratory and Los Alamos National Laboratory (1995).

[13] J.J. MacFarlane and P. Wang, *Phys. Fluids* **B3**, 3494 (1991).

[14] MacFarlane, J.J., Peterson, R.R., Wang, P., and Moses, G.A., *Fusion Technology* **26**, 886 (1994).

[15] MacFarlane, J.J., Moses, G.A., and Peterson, R.R., *Phys. Fluids* **B1**, 635 (1989).

[16] Peterson, R.R., in "Laser Interaction and Related Plasma Phenomena, Vol. 7," edited by H. Hora and G. Miley, Plenum Publ. Corp., p. 591 (1986).

[17] Peterson, R.R., *Fusion Technology* **13**, 279 (1988).

[18] Bailey, J.E., et al., in preparation (1995).

[19] MacFarlane, J.J., Wang, P., Chung, H.K., and Moses, G.A., "Spectral Diagnostics, Ion Stopping Power, and Radiation-Hydrodynamics Modeling in Support of Sandia Light Ion Beam Fusion Experiments," University of Wisconsin Fusion Technology Institute Report UWFDM-979 (April 1995).

[20] MacFarlane, J.J. and Cassinelli, J.P., *Astrophys. J.* **347**, 1090 (1989).

[21] Wang, P., "ATBASE Users' Guide," University of Wisconsin Fusion Technology Institute Report UWFDM-942 (December 1993).

[22] Melhorn, T.A. "A Finite Material Temperature Model for Ion Energy Deposition in Ion-Driven ICF Targets," SAND80-0038, Sandia National Laboratories, Albuquerque, NM, May 1980; also *J. Appl. Phys.* **52**, 6522 (1981).

[23] Kidder, R.E., *Nucl. Fusion* **16**, 3 (1976).

U.S. Department of Energy
Contract No. DE-AS08-88DP10754

The Development and Application of
Advanced Analytical Methods to
Commercial ICF Reactor Chambers

Task 3
Progress Report

Fusion Activation Code Development
as of September 29, 1995

Paul P.H. Wilson and Douglass L. Henderson

Fusion Technology Institute
University of Wisconsin-Madison

1. Background

The last 12 months has seen many changes in the development of a fusion activation code at the University of Wisconsin's Fusion Technology Institute. A new code, ALARA, has been developed from the old, GERAPH, which solves computational problems of memory allocation and speed while showing the same conceptual improvements. This report will describe some of the conceptual developments, both qualitative and quantitative as they apply to the new code, ALARA.

One year ago, the code under development was named GERAPH [Generalized Eigenvector Radioactivity Analysis for Pulsed Histories] and used some new techniques to perform the physical modelling and mathematical solution of the problem. While this code was functional, it was not always practical since, for large problems, it used excessive amounts of memory and was not sufficiently fast. In addition, the mathematical method while accurate and efficient, was complicated to implement.

Both of these problems pointed to the same solution. If a method could be developed to solve the problem in a set of linear chains, each created from the transmutation/decay trees, the memory requirement could be reduced and in many cases, when those chains did not include loops, the simple, well-known Bateman solution method could be used. Thus ALARA was born, a code with methodology similar to DKRICF's but with the allowance for loops in the transmutation/decay tree. These methodologies will be described in this report with specific reference to their implementation in ALARA.

2. Physical Modelling

2.1. Pruning the Trees and Untangling the Branches

While GERAPH's goal was to create a complete set of whole transmutation/decay trees before beginning computation, ALARA takes an entirely different approach. The trees are traversed in an approach known to computer scientists as a "depth-first search" to create linear chains of isotopes. The chains are extended until the truncation criteria are met at which point a solution is generated for all fine mesh intervals which contain that chain. The search continues creating new chains and solving them, one at a time. Thus, the storage requirements are reduced from the many thousands needed for a complete set of trees to approximately 10 for a single chain. This also leads to a corresponding drop in the storage requirements during the mathematical solution.

A common criticism of codes which rely on linear chains, however, is that they do not allow for loops in the transmutation/decay scheme. While there has been much debate as to the significance of this effect, work carried out during this development has pointed to the necessity for including loops.

When performing a simple qualitative analysis, as with many of the issues for activation codes (and any code for that matter), there is the argument that if it is possible to efficiently improve the physical model, there is little reason to not do so. It is, of course,

important to ensure that the benefit of improving the model is worth the time to do so. Thus quanititative analysis must be performed.

For this problem, an analysis was carried out to determine the effect of loops by incrementally adding corrections to the physical model. To understand the nature of these corrections, first consider a simple loop,

$$A \xrightarrow{(n,p)} B \xrightarrow{\beta^-} A.$$

If this loop is "straightened" an infinite linear chain of isotopes A and B would be created. Because of the nature of these transmutation/decay chains, each iteration of the $A \longrightarrow B$ loop can be considered a correction to the solution which ignores loops completely.

The analysis of this was conducted by extracting all the $(n,p) \rightarrow \beta^-$ loops which existed in the library and choosing a representative set of fusion material isotopes such as silicon, carbon, iron, etc., from this list. For each of these loops, the relative error between the approximate straightened loop solution and the exact analytical solution was computed for 0 through 5 corrections, where 0 corrections indicates that the loop is being ignored completely. The solutions were computed for pulsing schemes representative of reactor operation for equally spaced total operating lifetimes on a logarithmic scale from 10^4s to 10^{10}s. The results, as shown in Figures 1 and 2, indicate that ignoring the loop can introduce error as high as 0.2%, particulary for long operating lifetimes. It also demonstrated, however, that a small finite number (1 to 3) of corrections is needed to reduce this error to below 10^{-8}. Since these errors are relative errors, they indicate the accuracy of the result and not its precision. Thus, regardless of the expected production rate of an isotope which may be involved in a loop, this relative error indicates the maximum number of significant digits of the result. Since most input data and parameters rarely have more than 5 or 6 significant digits, the relative error need only be less than 10^{-7} to prevent this loop approximation from affecting the accuracy of the results.

But why not use the exact physical model at all times? When the exact model is used, it requires the use of methods which are complicated, difficult to implement, and introduce error during the mathematical solution. Linear chains with straightened loops, on the other hand, allow for simple and accurate mathematical methods, accelerating the development of the code and speed of the solution. Furthermore, it allows the code to adaptively choose a solution method, depending on the nature of the chain, which can be more efficient and/or more accurate.

To determine how many corrections are necessary, ALARA uses the same truncation criteria for these straightened loops as it does for all other chains, thus ensuring that the precision of the solution for the chains which contain loops is the same as those which do not.

2.2. Cutting Back the Growth

An important, but less contentious, issue is that of chain truncation. The existence of large and extensive modern activation libraries would result in nearly infinite chains if left

unchecked. Thus some method must be developed to truncate those chains without having significant effect on the accuracy or precision of the answer.

A qualitative analysis of this issue gives rise to a simple set of truncation rules which rely on a precision tolerance chosen by the user. As each chain is created, a reference calculation is performed to determine the relative production of the bottom isotope from the top, initial isotope. If this value falls below the user-specified tolerance, the chain is truncated at that point. Any such truncation results in an apparent loss of atoms from the system since the bottom isotopes in these chains might decay or be transmuted, but by setting the truncation tolerance at a low value, this can be minimized.

This apparent "loss of atoms" can increase, however, if the chains are truncated on radioactive isotopes which may have an opportunity to decay for many half-lives during the after-shutdown analysis period. Thus, an additional criterion is added to prevent the truncation of the trees on a radioactive isotope.

It is possible, however, to have radioactive isotopes for which cross section data exists. If it is determined that an isotope such as this should be a point of truncation, it would be saved from truncation by the above criterion and the chain would be extended. A number of these isotopes in succession can lead to extremely long chains with negligible production rates. It is therefore necessary to define a third alternative to complete truncation and complete non-truncation. That is, if such a situation occurs, only the decay daughters of the offending isotope will be followed, a condition which is inherited by each of these daughters. Thus, a chain can only end on a stable isotope, but non-decay reactions will be ignored once the relative production criterion has failed.

3. Mathematical Modelling

3.1. Back to Basics

Throughout this code development, there has been the assumption that the solution would be carried out with a matrix method, thus increasing the speed of the solution. GERAPH tackled this problem by exploring the basic method for the solution of the matrix exponential with degenerate eigenvalues. This method relied on the use of generalized eigenvectors which had to be determined by a complicated series of mathematical routines. In addition, it attempted to solve the entire tree at one time, so that if there was a single loop in a tree of many hundred isotopes, the complicated solution method would be applied to the whole problem. Even during shutdown periods, the method was complicated by the size of the matrix.

Once the transmutation/decay trees have been modelled as a set of linear chains, potentially containing straightened loops, the mathematical problem becomes greatly simplified. All isotopes in the chain have a potential contribution from all those above them in the chain, thus ensuring a full lower triangular matrix in the solution. Furthermore, the form of the contribution of one isotope, k, to another, i, is the same for all pairs of

isotopes, independent of the existence of a loop, when written in Laplace transform space:

$$\tilde{N}_{i,k}(s) = N_{k_o}\tilde{F}_{i,k}(s)\prod_{j=k}^{i-1} P_{j\rightarrow j+1}$$

where

$$\tilde{F}_{i,k}(s) = \prod_{j=k}^{i}\frac{1}{s+d_j},$$

$P_{j\rightarrow j+1}$ is the total production rate from isotope j to isotope $j+1$ and d_j is the total destruction rate of isotope j.

When the $P_{j\rightarrow j+1}$ and d_j are unique due to the absence of loops in a particular chain, the inverse transform of this is trivial and is the Bateman solution. In addition, during decay periods, such as between pulses and after-shutdown, loops are not possible and the Bateman method can be used even when loops do exist during the irradiation time. Since for each chain's solution, there is a single irradiation transfer matrix but many decay transfer matrices to be calculated, this is a great advantage since the majority of the calculation will involve the well tested Bateman solution.

When there are loops during the irradiation time, it is necessary to find the inverse of this transfer function, $\tilde{F}_{i,k}(s)$. Two methods to perform this calculation have been developed and implemented.

3.2. Basic Math: Two Computational Solutions to the Laplace Inversion

The first method for solving this inverse transform is to take each unique pole, d_j, determine its multiplicity, and determine the partial fraction expansion for this pole. This is a fairly simple operation to perform with pen and paper, and an algorithm was developed to carry this out computationally.

For multiplicities, m_j, greater than 1 (caused by straightened loop corrections), derivatives of the function

$$\tilde{G}^{j}_{i,k}(s) = (s+d_j)^{m_j}\tilde{F}_{i,k}(s)$$

evaluated at $s = -d_j$ are required. Careful analysis has shown that these derivatives can be calculated using a simply recursive formula which is easily implemented. These residues are then used to perform the partial fraction expansion and subsequent inversion of the Laplace transform arriving at the contribution to isotope i from isotope k.

The second method for solving this inverse transform is to convert this function $\tilde{F}_{i,k}(s)$ into a power series in $\frac{1}{s}$ as follows:

$$\begin{aligned}
\tilde{F}_{i,k}(s) &= \prod_{j=k}^{i} \frac{1}{s+d_j} \\
&= \frac{1}{s^{i-k+1}} \prod_{j=k}^{i} \frac{1}{1+\frac{d_j}{s}} \\
&= \frac{1}{s^{i-k+1}} \prod_{j=k}^{i} \left[1 - \frac{d_j}{s} + \frac{d_j^2}{s^2} - \frac{d_j^3}{s^3} + \frac{d_j^4}{s^4} + \cdots\right] \\
&= \frac{1}{s^{i-k+1}} - \frac{\sum_{j=k}^{i} d_j}{s^{i-k+2}} + \frac{\sum_{j=k}^{i} d_j \sum_{l=j}^{i} d_l}{s^{i-k+3}} - \cdots
\end{aligned}$$

In situations where the destruction rates are adequately small, this method will be accurate if enough terms are kept in this expansion. It is also a straightforward and efficient way to determine the contribution of isotope k to isotope i at any time.

4. Where We Are and Where We Are Going

The new code, ALARA [Adaptive Laplace and Analytic Radioactivity Analysis], is currently in the final stages of development and testing with the above mentioned functionality. In this process of development, it is being designed for accuracy, efficiency (speed) and ease of use.

When completed, ALARA will provide output in a number of formats to enable thorough analysis of the problem. In addition to giving the number densities of all the isotopes which are determined to be in the decay/transmutation chains, it will provide the activity of all radioactive isotopes, the decay afterheat, the BHP, the gamma source, and even the dose at a point, if requested. Furthermore, that information can be provided at a variety of spatial resolutions including both fine and coarse mesh intervals and entire mixtures. Finally, the code will be able to interface with the standard transport code data files to ease the transition from transport calculations to activation calculations.

The future work for activation code development includes implementation of further enhancements such as pathway analysis and sensitivity analysis. In addition, the additional activation from sequential reactions will be accounted for and the adjoint method will be developed, allowing users to pinpoint particular isotopes and directly determine their production rate from the initial isotopes.

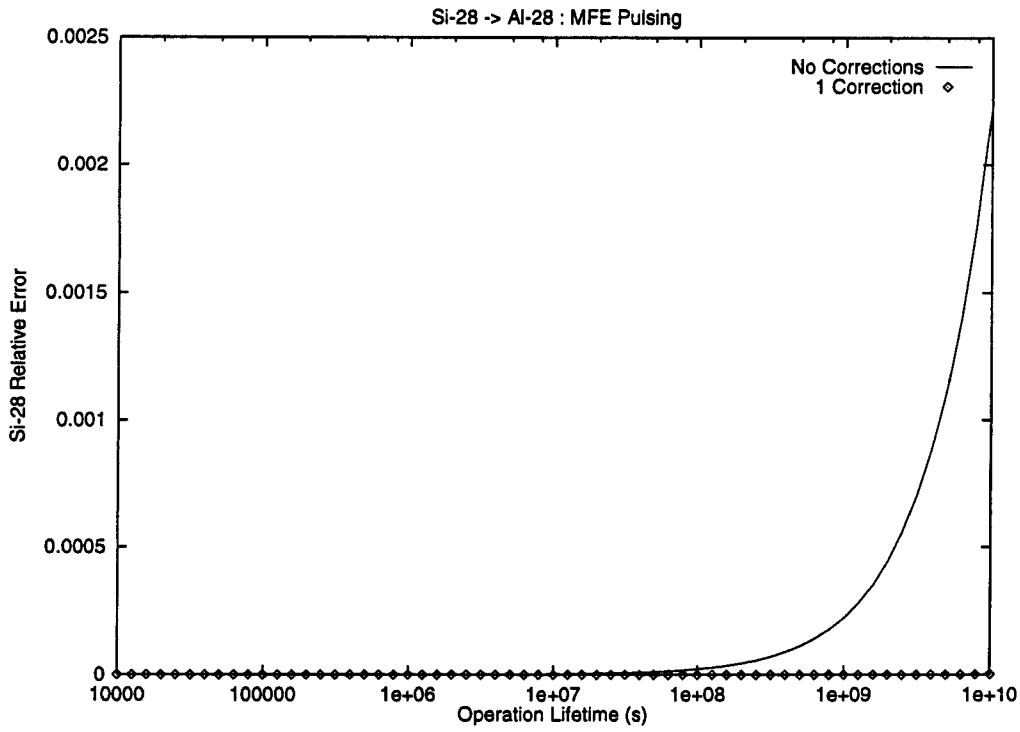

Figure 1: Relative error in production rate of ^{28}Si for $(n,p) -> \beta^-$ loop involving ^{28}Si and ^{28}Al

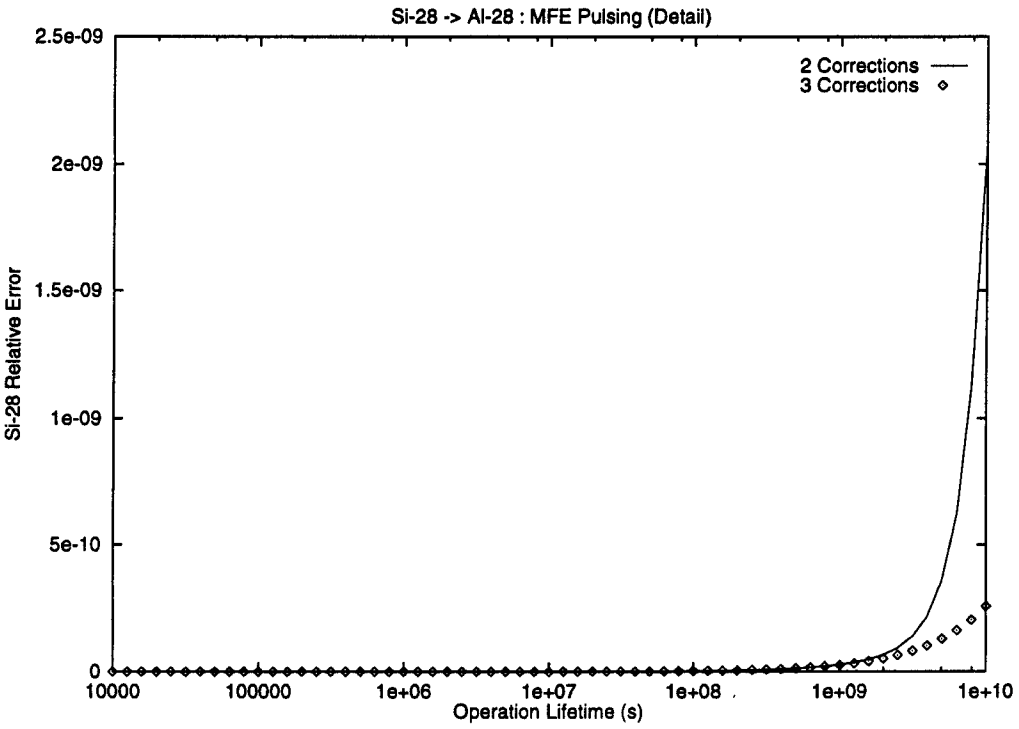

Figure 2: Detailed information for relative error in production rate of ^{28}Si for $(n,p) -> \beta^-$ loop involving ^{28}Si and ^{28}Al

U.S. Department of Energy
Contract No. DE-AS08-88DP10754

The Development and Application of
Advanced Analytical Methods to
Commercial ICF Reactor Chambers

Task 4
Progress Report

Structural Dynamics Modeling of ICF Reactor Chambers

R. Engelstad

P. Cousseau
C. Nin

Fusion Technology Institute
University of Wisconsin - Madison

I. Introduction

The design of an inertial confinement fusion (ICF) reaction chamber involves identifying the structural response of the containment vessel to intense thermal and mechanical loads as energy is released from the implosion. The Fusion Technology Institute (FTI) has been involved with a number of ICF reactor designs over the last fifteen years. The response of the first wall to an impulsive pressure or thermal shock is a critical issue and has been included in nearly all of the reactor designs. The primary mechanism for simulating the mechanical response of the chamber has been numerical computer codes developed for each of the individual designs. The intent of this research is to extend existing programs and generate new codes in parametric form so that software packages can be made available to the ICF community. Consequently, the user may easily change geometry, materials, boundary conditions or loading conditions to arrive at the final design.

The code development effort has been divided into the following three areas:

A.) Cylindrical Shells
B.) Spherical Shells
C.) Reactor Components (Beam Tubes, Cooling Tubes, etc.)

The work that has been completed in each of these areas is presented in this progress report.

II. Cylindrical Shells

Previous Investigations

Many investigators have developed the differential equations of motion which describe the behavior of thin shells. An extensive publication by Leissa [1] is a compilation of a wealth of information about shell vibrations, primarily cylindrical shells. Ludwig and Krieg [2] considered the effect of various boundary conditions on the flexural vibration characteristics, including axisymmetric cases, using quasi-exact methods. Since the loading of the reaction chamber is primarily axisymmetric, only the response to this type of excitation will be considered in the code development work.

More recently, Adler [3] used a variety of boundary conditions on a cylindrical shell to show their effects on frequencies and mode shapes. He showed that boundary conditions can affect cylindrical shell frequencies and mode shapes in unexpected ways. Natural frequencies change only slightly when various end conditions are applied, although mode shapes can vary greatly. The addition of axial restraint has a strong influence on the mode shapes, and complications can arise due to "double modes" or the occasional superposition of a mode shape at one frequency with the mode shape at nearby frequencies.

Problem Formulation

Initially, a finite model of a thin cylindrical shell with no holes was created to compare with previous studies and known analytical solutions. The analytical solution for a thin cylindrical shell is extremely difficult and computationally intensive to solve. No known analytical solution exists for thin cylindrical shells with perforation patterns.

Figure 1 shows the schematic of a cylindrical shell with the axial, circumferential and radial directions denoted by x, θ and r, respectively. The corresponding displacements are given

by u, v and w. In addition, the shell dimensions are given by the following: h is the thickness, a is the radius, and l is the length.

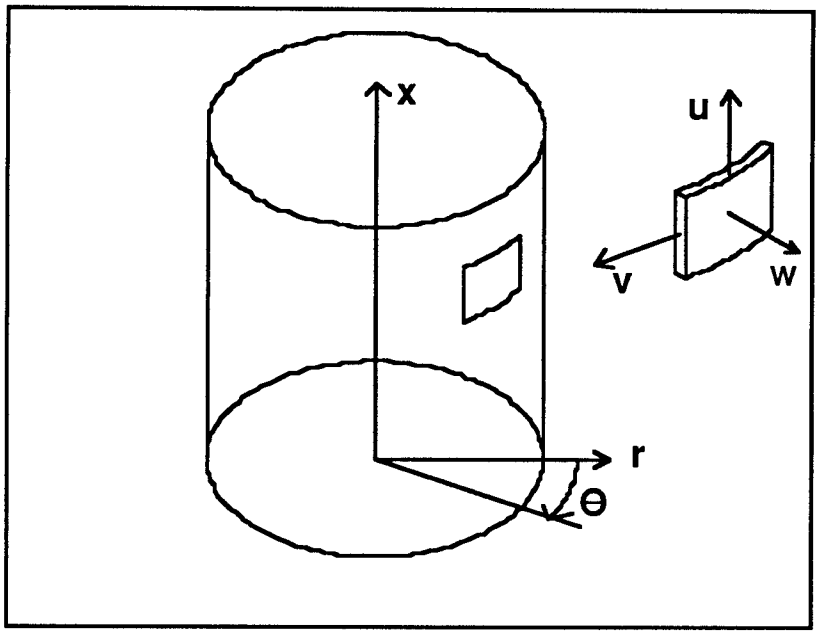

Figure 1. Cylindrical coordinate system and displacement components.

There are many different formulations of the general differential equations of motion for thin shell vibrations (Love, Flugge, Timoshenko, etc.). The analyses follow the common assumptions of linear thin shell theory proposed by Love [4], i.e., the cylinder is assumed to be thin (a/h>10), of constant wall thickness and made of a linear, isotropic, homogeneous material. The equations as developed by Flugge [5] are:

$$\frac{\partial^2 u}{\partial x^2}+\frac{1-\upsilon}{2}(1+k)\frac{\partial^2 u}{\partial \theta^2}+\frac{1+\upsilon}{2}\frac{\partial^2 v}{\partial x \partial \theta}-k\frac{\partial^3 w}{\partial x^3}+\frac{1-\upsilon}{2}k\frac{\partial^3 w}{\partial x \partial \theta^2}+\nu\frac{\partial w}{\partial x}-\gamma^2\frac{\partial^2 u}{\partial t^2}=0$$

$$\frac{1+\upsilon}{2}\frac{\partial^2 u}{\partial x \partial \theta}+\frac{\partial^2 v}{\partial \theta^2}+\frac{1-\upsilon}{2}(1+3k)\frac{\partial^2 v}{\partial x^2}-\frac{3-\upsilon}{2}k\frac{\partial^3 w}{\partial x^2 \partial \theta}+\frac{\partial w}{\partial \theta}-\gamma^2\frac{\partial^2 v}{\partial t^2}=0$$

$$-k\frac{\partial^3 u}{\partial x^3}+\frac{1-\upsilon}{2}k\frac{\partial^3 u}{\partial x \partial \theta^2}+\nu\frac{\partial u}{\partial x}-\frac{3-\upsilon}{2}k\frac{\partial^3 v}{\partial x^3}+\frac{\partial v}{\partial \theta}+(1+k)w+2k\frac{\partial^2 w}{\partial \theta^2}+k\nabla^4 w+\gamma^2\frac{\partial^2 w}{\partial t^2}=0$$

where

$$\gamma^2=\frac{\rho a^2\left(1-\upsilon^2\right)}{E}$$

$$k=\frac{h^2}{12a^2}$$

$$\nabla^2=\frac{\partial^2}{\partial x^2}+\frac{\partial^2}{\partial \theta^2}$$

These differential equations can be combined together in w, resulting in a single 8th order differential equation. Ludwig and Krieg developed quasi-exact eigensolutions for Flugge's differential equations for linearly elastic, thin cylindrical shells (using separation of variables), matching the boundary conditions at each end of the cylinder and introducing a harmonic solution.

In the case of axisymmetric vibrations, the differential equations can be separated, or decoupled, from an 8th order equation to a 6th order and a 2nd order equation. Ludwig and Krieg introduced a quasi-exact method of evaluating the eigensystem of the 6th order differential equation. The natural frequencies and mode shapes are determined by substituting the boundary conditions into the following differential equation:

$$\frac{d^6 W_{m0}}{dx^6} + K_{4m0}\frac{d^4 W_{m0}}{dx^4} + K_{2m0}\frac{d^2 W_{m0}}{dx^2} + K_{0m0} W_{m0} = 0$$

where

$$K_{4m0} = 2\left(\Omega_{m0}^2 + \frac{\upsilon}{1-k}\right)$$

$$K_{2m0} = \Omega_{m0}^4 - \frac{1-2\upsilon k}{k(1-k)}\Omega_{m0}^2 + \frac{1-\upsilon^2+k}{k(1-k)}$$

$$K_{0m0} = \frac{1+k-\Omega_{m0}^2}{k(1-k)}\Omega_{m0}^2$$

and Ω_{mn} is the dimensionless eigenfrequency. This is the equation of motion that is solved to verify the finite element modeling.

Finite Element Modeling and Verification

A three dimensional finite element model of a thin cylindrical shell with no perforations was created. This model matched the numerical solution for the natural frequencies and mode shapes for a variety boundary conditions. The numerical results were obtained by solving the 6th order differential equation using a method developed by Ludwig and Kreig. The finite element data also matched the experimental data from Adler [3] and a number of examples from Leissa [1]. Consequently, the type of finite element used in the model and the meshing density were benchmarked.

A second finite element model (see Figure 2) was then generated with a square perforation pattern. For this case, the input file was created in parametric form allowing the user to specify the dimensions of the cylinder, the size of the perforations and the specific pattern. The meshing is then completed according to the input parameters. For the specific case shown in Fig. 2, the natural frequencies and mode shapes were calculated, and the results were very close to the case with no perforations.

It should be noted that the finite element input file has been created in such a manner that the perforations may be circular or elliptical, and can they can be arranged in rows and columns in either a square or triangular pattern. The perforations may have reinforcement around the edges, and the reinforcement may be made from a different material. In addition, the dimensions of the holes may be changed for each row.

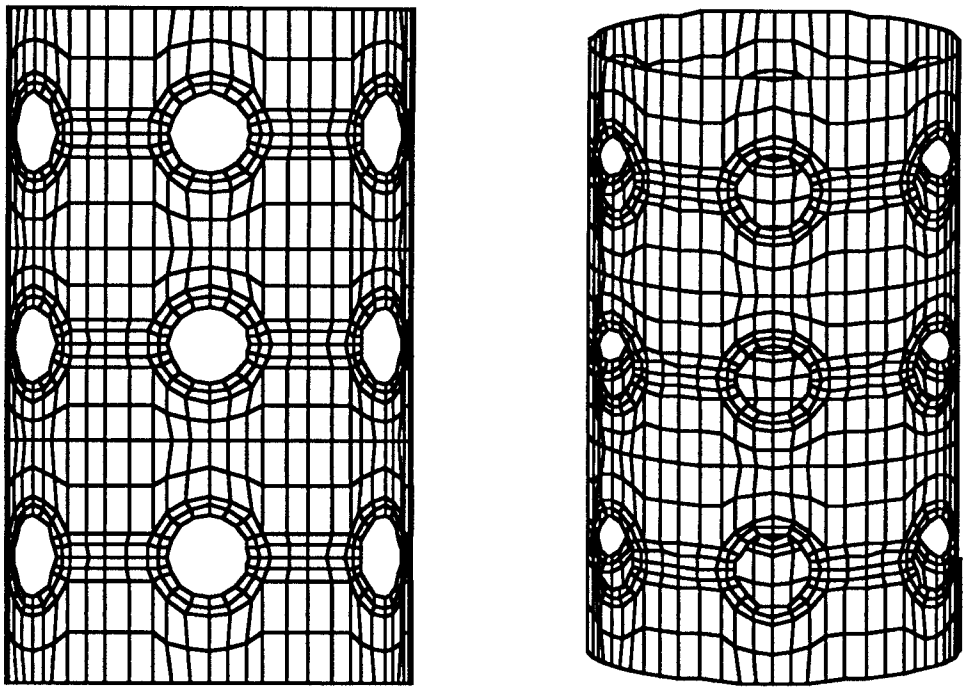

Figure 2. Finite element model with square perforation pattern.

Future Work

Code development will continue to ensure that the input files for the cylindrical shells are as generic as possible. The models will also be expanded to include optional boundary conditions at the edges of the perforations and the addition of end caps. The models will still need to be verified with theory for relatively "short" shells.

Thus far the finite element models have all been developed for a modal analysis solution within the commercial code ANSYS. A transient solution type is being benchmarked in order to simulate the dynamic response of the blast wave and identify the regions under the highest stress.

III. Spherical Shells

Introduction

Spherical shells have also been proposed to be used as containment vessels for inertial confinement fusion, for example in NIF. Determining the structural response (i.e., the location of maximum displacement and stresses) of spherical shells with perforations subjected to repetitive thermal and mechanical loads released from the implosion is necessary for the successful design of a ICF reactor. Analytical solution for the axisymmetric natural frequencies for a homogenous, continuous sphere can be found in the literature [6, 7]. These analytical

solutions can be used to benchmark more complicated finite element models, such as spherical shells with perforations for laser beams and target injection.

Finite Element Modeling and Verification

An axisymmetric finite element model of a spherical shell has be created using the commercially available program ANSYS. This model includes membrane and bending stress, and boundary conditions can be added where they are needed. The analytical equation for the torsionless natural frequency based on bending theory can be found in [6] and the torsional natural frequency equation based only on membrane theory can be found in [7]. For both of these solutions, it is necessary to idealize the problem such that no support forces (i.e., boundary conditions) are applied to the spherical shell. Table 1 compares the analytical and finite element torsionless natural frequencies and Table 2 compares the torsional natural frequencies. The finite element model is in very good agreement with the analytical solutions. Mode 1 of Table 1 is the "breathing" mode of the sphere. This is the mode that will be predominately excited from a uniform blast wave emanating from the center of the sphere.

Table 1. Natural frequencies of the first three modes of torsionless vibration dominated by in-plane motion for the following parameters: $a = 1$ m, $h = 0.02$ m, $E = 216$ GPa, $\upsilon = 0.3$, $\rho = 7800$ kg/m^3.

Mode Number	Analytical Solution [Hz] (Bending Theory)	FEM Solution [Hz] (Axisymmetric Model, 201 Nodes)
1	1415.7	1415.7
2	1733.9	1733.8
3	2389.9	2389.8

Table 2. Natural frequencies of the first three torsional modes for the following parameters: $a = 1$ m, $h = 0.02$ m, $E = 216$ GPa, $\upsilon = 0.3$, $\rho = 7800$ kg/m^3.

Mode Number	Analytical Solution [Hz] (Membrane Theory)	FEM Solution [Hz] (Axisymmetric Model, 201 Nodes)
1	1038.7	1038.9
2	1642.4	1642.7
3	2203.5	2204.1

An analytical solution based on membrane theory and a numerical implementation of the solution has been completed to simulate the dynamic response of an axisymmetric spherical shell to uniform sequential impulses. It is assumed that the shell is thin and will be uniformly excited by the bast loading. A single mode solution using the "breathing" mode has been used for this solution. The intent here is to use this numerical solution to benchmark the finite element models.

In addition, the stresses resulting from a static pressure load on a hemispherical cap have been benchmarked with known analytical solutions [8]. Figure 3 shows a model of a hemispherical cap with simply-supported edge conditions (allowing radial displacement). When a static pressure load (uniform over the external surface) is applied the resulting stress contours

can be computed (see Figure 4). For the mesh density shown, the percent error of the FEM calculations for the circumferential stress is 2.5%.

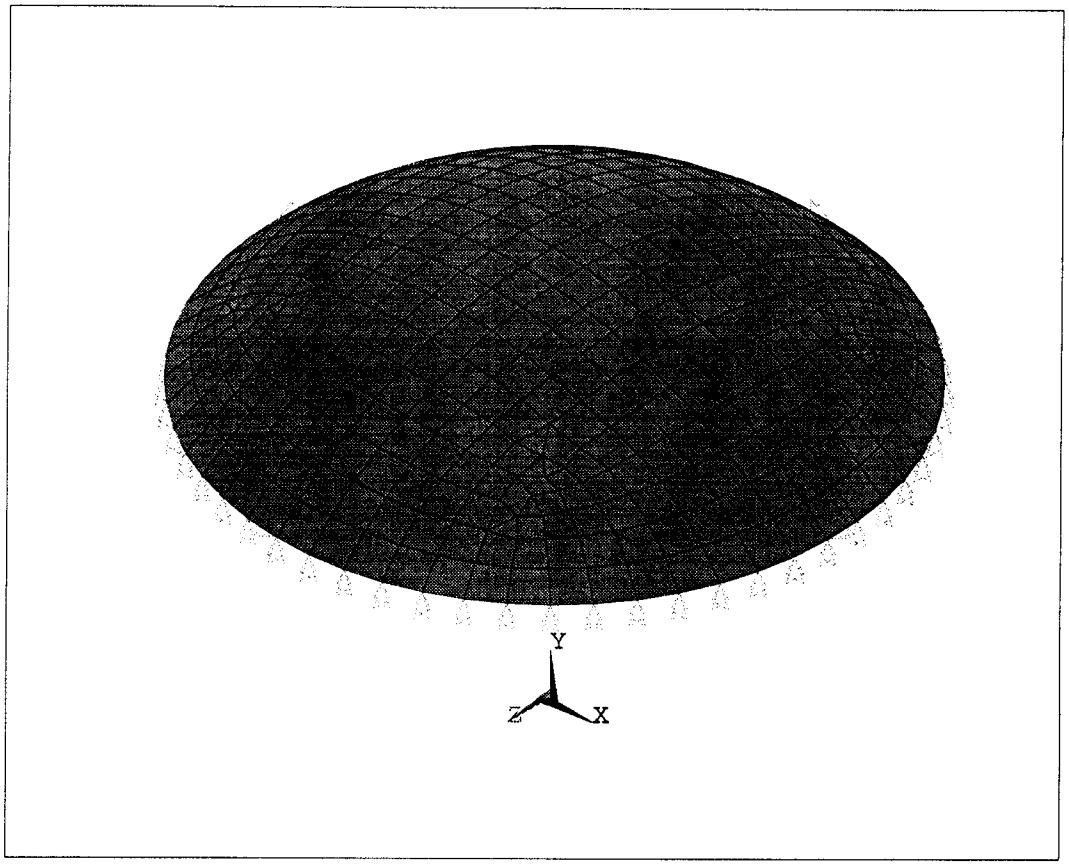

Figure 3. A finite element mesh of a hemispherical cap with simply-supported edge conditions.

Results and Future Work

The natural frequencies of an axisymmetric spherical shell and a hemispherical cap have been benchmarked and are in full agreement with the analytical solutions. Future work includes, developing for a spherical shell a finite element model employing cyclic symmetry and a full 360° model. These models can be benchmarked using the same analytical solutions described above.

IV. Reactor Components

A major problem in ICF reactor design is the protection of the first wall from x-rays, neutrons, target debris and mechanical shock resulting from target ignition. The concept of protecting the cylindrical cavity by an annular bank of vertical tubes conveying liquid lithium/lead has been proposed in a number of reactor designs, i.e., HIBALL and LIBRA. A set

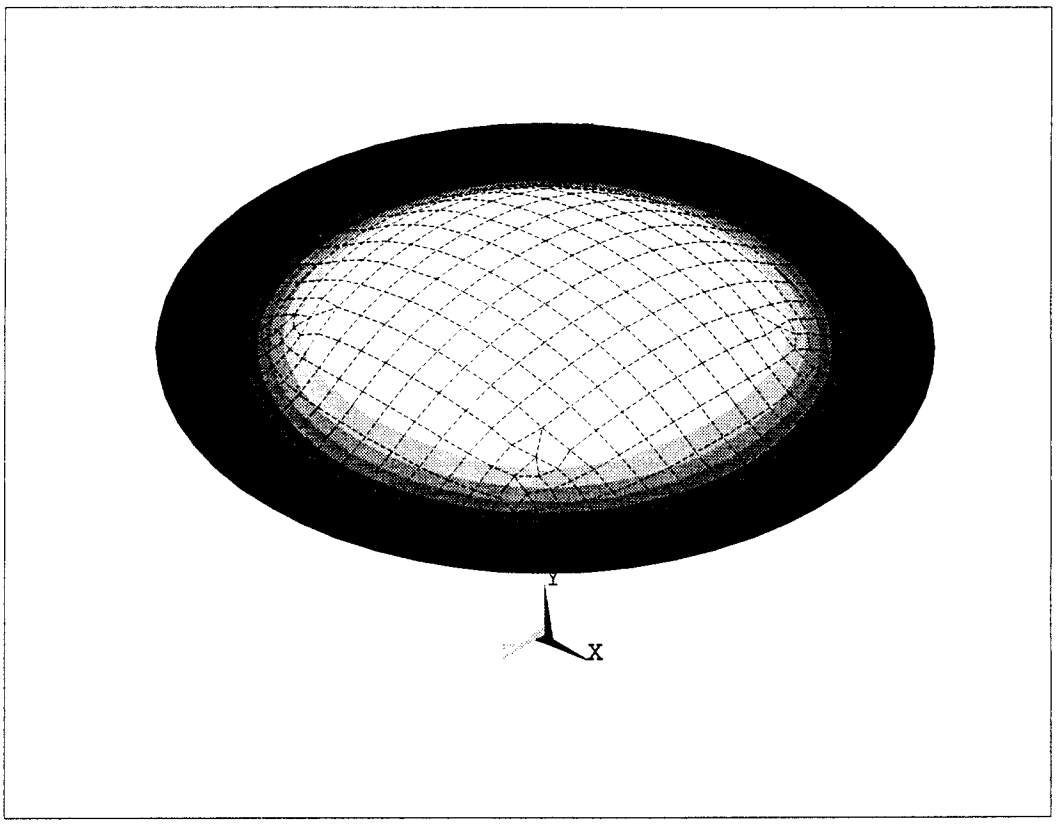

Figure 4. Stress contours for a simply-supported hemispherical cap with a static pressure load uniformly distributed over the external surface.

of five different computer codes have been developed to model the vertical tube's response to planar impulsive excitations. A brief description of each code is given below:

- **B-Tube** (Braided Tube):
  A braided silicon carbide tube conveying liquid coolant is modeled as a tube with no bending stiffness but having a constant internal fluid flow. The hollow "string-like" model is preloaded with an axial tension to provide the structural load carrying capability. The nonplanar, nonlinear equations of motion were previously derived by Engelstad [9]. Numerical integration routines have now been written to solve the differential equations of motion and simulate the tube response to sequential impulses. The code's adjustable parameters include the repetition rate of the reactor (i.e., the period of the sequential impulses), the excitation magnitude, the velocity of the internal fluid, the damping in the system and the geometry of the tube. The code reports data for the midspan displacement of the tube as a function of time. With this data both the steady state and transient response of the tube can be studied. Also, the amplitude-frequency relationships identifying resonance conditions can be determined. With this code, it has been shown that the primary response of the tube will be a radial displacement (or planar displacement), however, the tubes could begin to "whirl" under certain operating conditions.

- **E-Tube** (Extensional Tube):
  This code models an "elastic" tube clamped at both ends conveying a liquid coolant while subjected to planar sequential impulses. In this case, the tube has an actual bending stiffness so no preload axial tension is needed. It is also assumed that the clamped end conditions are rigidly fixed and the length of the tube will extend during oscillatory motion. The nonplanar, nonlinear equations of motion were previously derived by Lee [10]. A computer code has now been generated to simulate the dynamic response of the tube. The adjustable parameters and data output are similar to the B-Tube code. This code also demonstrates that the tube could enter "whirling" motion under certain operating conditions.

- **I-Tube** (Inextensional Tube):
  The I-Tube code package is similar to the nonlinear E-Tube code with clamped boundary conditions that move freely in the axial direction. Consequently, longitudinal deformation does not occur. Again, the nonplanar, nonlinear equations of motion were previously derived by Lee [10]. The adjustable parameters and data output are similar to the B-Tube code.

- **S-Tube** (Stress Tube):
  This code models the planar displacement and bending stress in a elastic tube with arbitrary boundary conditions conveying liquid coolant subjected to planar sequential impulses. A major feature of this code is that the stress and displacement histories for any location along the length of the tube can be calculated, in contrast to the above three codes where only displacement at the center of the tube is returned. Another feature of the program is the ability to easily model any combination of classic boundary conditions; for example pinned-pinned, clamped-clamped, pinned-clamped; by using their associated orthogonal shape functions.

  The general equation of motion describing the planar mechanical response of a tube under sequential impulse loading can be found in [11]. A modal solution of the equation of motion for arbitrary boundary conditions is also given. This solution was programmed in the S-Tube code. In the above derivation the following assumptions were made. The pressure load is assumed to be uniformly distributed over the length of the tube, is impulsive in nature and is applied at the rep rate of the reactor. Since the flow velocity of the liquid coolant is small, the effects of moving liquid within the tube can be neglected and the fluid considered stationary. Stationary fluid in a tube adds mass to the system without change the flexural rigidity of the tube. Rayleigh damping was used to model internal structural damping and external viscous damping. The code's adjustable parameters include the repetition rate of the reactor, the excitation magnitude, the tube geometry, and the material properties of the tube and liquid coolant.

  Figure 5 shows for particular input parameters the absolute maximum steady state midspan displacement of a clamped-clamped tube as a function of sequential impulse frequency. This figure illustrates the frequencies or repetition rates associated with resonant conditions, i.e., the peaks in the response curves. The large peak in the center of the figure is the fundamental frequency of the system and the peaks to the left are overtones of the fundamental frequency. These peaks would effectively shift as the length of the tube changes. Therefore, this program can be used to establish the free span tube length in order to place the reactor's operating rep rate away from the resonant peaks.

• **FEM-Tube** (Finite Element Model):
A finite element model of a tube conveying coolant fluid under sequential impulse loading was also constructed using the commercially available program ANSYS. The finite element model confirms the displacement and stress results from the above analytical solutions. Figure 6 compares the transient displacement of a pinned-pinned tube subjected to sequential impulses at a frequency of 3.8 Hz.

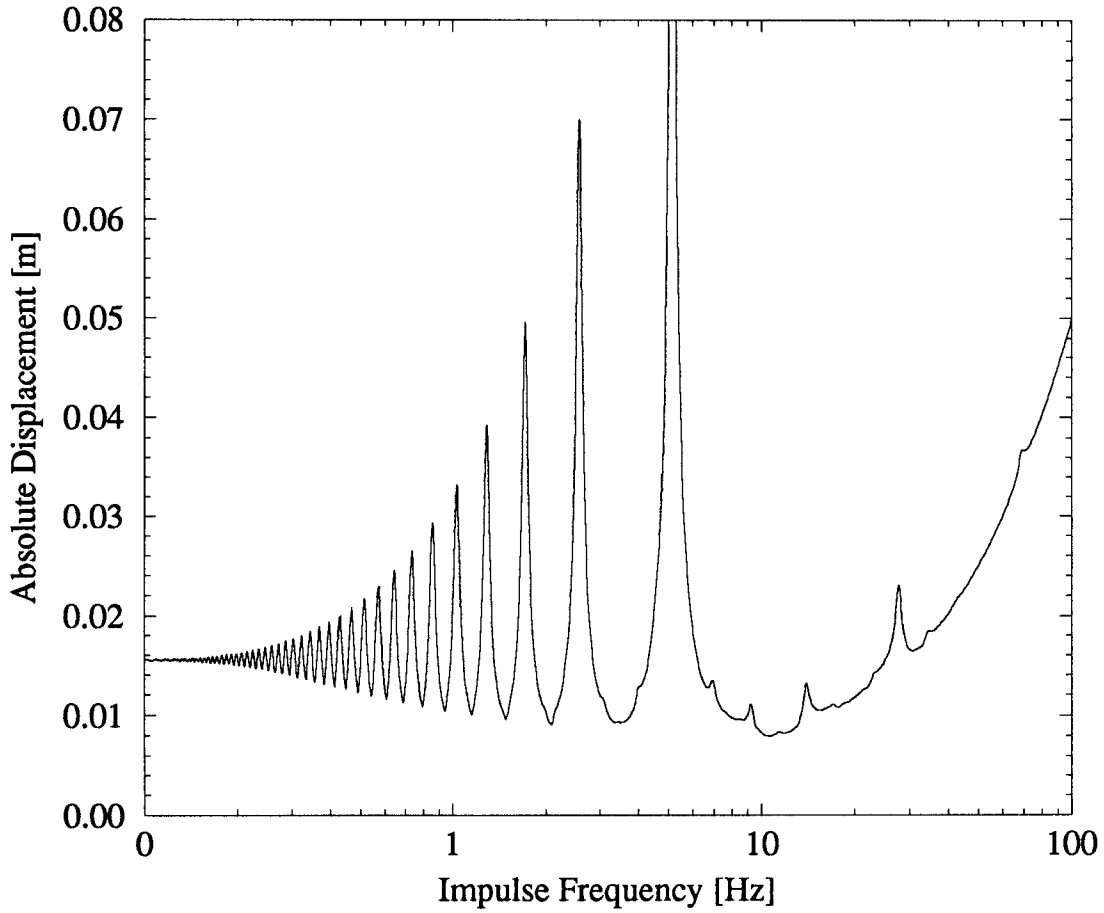

Figure 5. Absolute maximum steady state midspan displacement of a pinned-pinned tube driven by sequential impulse frequency.

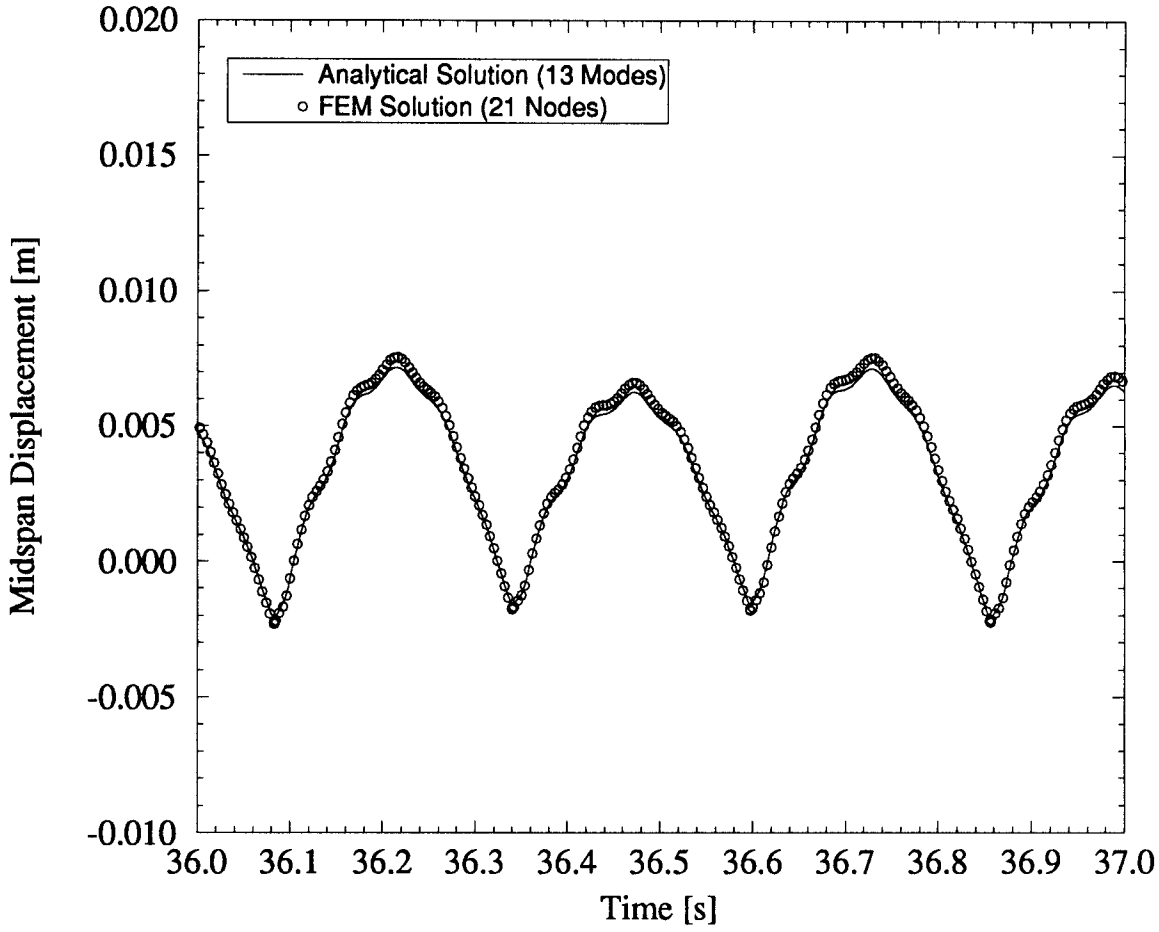

Figure 6. Comparison between the analytical S-Tube code and a FEM-Tube code.

V. References

[1] Leissa, A. W., *Vibrations of Shells*, NASA SP-288, 1973.

[2] Ludwig, A. and Krieg, R., "An Analytical Quasi-Exact Method for Calculating Eigenvibrations of Thin Cylindrical Shells," *Journal of Sound and Vibration*, Vol. 74, No. 2, 1981, pp. 155-174.

[3] Adler, D.P., "The Effect of End Conditions on the Axisymmetric Vibrations of Cylindrical Shells," Master's Thesis, University of Wisconsin-Madison, 1993.

[4] Love, A. E. H., A Treatise on the Mathematical Theory of Elasticity, Dover, New York, 1944.

[5] Flugge, W., *Stresses in Shells*, Springer-Verlag, Berlin, 1960.

[6] Soedel, W., *Vibrations of Shells and Plates*, Marcel Dekker, Inc., New York, 1993.

[7] Blevins, R.D., *Formulas for Natural Frequency and Mode Shape*, Robert E. Krieger Publishing Co., Malabar, Florida, 1987.

[8] Cook, R. and Young, W., *Advanced Mechanics of Materials*, Macmillan Publishing Co., New York, 1985.

[9] Engelstad, R. L., "Vibration and Stability of Vertical Tubes Conveying Fluid Subjected to Planar Excitation," Ph.D. Thesis, University of Wisconsin - Madison, 1988.

[10] Lee, Y.-M., "Nonlinear Vibration and Stability of a Beam Subjected to Planar Excitations," Ph.D. Thesis, University of Wisconsin - Madison, 1994.

[11] B. Badger et al., "LIBRA-SP - A Light Ion Fusion Reactor Design Study Utilizing a Self-Pinched Mode of Ion Propagation, Report for the Period Ending June 30, 1995," University of Wisconsin Fusion Technology Institute Report UWFDM-982, June 1995.

U.S. Department of Energy
Contract No. DE-AS08-88DP10754

The Development and Application of
Advanced Analytical Methods to
Commercial ICF Reactor Chambers

Task 5
Progress Report

Cavity Clearing

E. A. Mogahed

Fusion Technology Institute
University of Wisconsin-Madison

I. Introduction

In Inertial Confinement Fusion (ICF) reactors, the performance of the reactor cavity is of paramount importance to the overall qualification of the reactor. Controlling the initial conditions of the gas in the reactor cavity prior to every microexplosion is the key to many crucial aspects related to the performance of the reactor cavity. The immediate pre-explosion gas pressure and the concentration (mass density) of different species in the reactor cavity atmosphere have a strong direct effect on the efficiency and performance of the reactor.

Predicting the initial conditions of the gas in the reactor cavity prior to every microexplosion with a reasonable degree of accuracy is highly desirable to insure a successful reactor design. Clearing the products of the microexplosion (condensable vapors, noncondensable gases, target fragments, etc.) is normally achieved by either self-pumping of the high pressure/temperature gases through ports in the reactor cavity walls or by mechanical evacuation. These ports are usually connected to a large dumping tank. Hard vacuum pumps are connected to the dumping tank to assure constant low pressure during reactor operation. There is a major additional contribution from the vapor condensation process either in droplet form or from thin film condensation on various cold surfaces in the cavity. The dynamics of this system from the time of target explosion until the time of next explosion (this period of time is proportional to the reciprocal of repetition rate) is the subject of this work.

The goals of this project are to:

1. Analyze the transient hydrodynamics of the clearing system.
2. Evaluate the effects of the evaporation and recondensation of the first wall and target materials.
3. Evaluate the needed rate of pumping.
4. Develop a high performance computational computer code to address these issues.

II. Background

The cavity atmosphere is primarily dictated by the requirements needed to propagate the beams to the target with minimum loss due to stripping and charge exchange. The equilibrium pressure of the noncondensable gases (D_2, T_2, and He, Ar, Xe,..., etc.) has to be maintained reasonably low, although its effect on beam propagation is not as great as the vapor of liquid or solid metals at the same number density. Furthermore, the noncondensable partial pressure has to be kept low because it constitutes a continuous source of molecules migrating into the beam lines where the pressure must be kept at a very low value depending upon whether heavy ion, light ion, or laser drivers are used.

Immediately after a shot, the gas pressure in the cavity reaches as high as 100 torr. Immediately near the cavity inner surfaces the local pressure exceeds that value of pressure by many orders of magnitude due to the vaporization of the surface material in the case of dry wall designs or due to the vaporization of the liquid metals for designs using wetted walls. Due to rapid expansion near the wall droplet formation is expected and the internal surfaces of the cavity act as a condenser for the remainder of the condensable vapors. Accurate prediction of the condensation state either on the cold cavity internal surfaces or in the form of droplets is required to insure that the condensation is rapid enough to achieve the desired repetition frequency of several hertz.

III. Problem Formulation

The issue of metal vapor condensation, either from the wetted or dry wall concept, may be divided into two fundamental problems:

1. Liquid film condensation on the rather cold surfaces of the cavity interior.
2. Homogeneous droplet nucleation in a supersaturated vapor within the body of the gas-vapor mixture inside the cavity.

The two fundamental problems will be addressed briefly in the next discussion.

In the previous report the homogeneous droplet nucleation has been discussed. In this part of the report the liquid film condensation on the rather cold surfaces of the cavity interior will be our focus.

IV. Heterogeneous Nucleation in Vapor

In most applications involving condensation, the process is initiated by removing heat through the walls of the structure containing the vapor to be condensed. In our present case the microexplosion provides enough energy to heat up the gas in the cavity and to evaporate some of the liquid metal coolant. If enough heat is removed by the coolant, the vapor near the rather cold wall may be cooled below its equilibrium saturation temperature for the specified system pressure. Since the heat removal process will establish a temperature field in which the temperature is lowest right at the wall of the containment, the formation of a liquid droplet embryo is most likely to occur right on the solid-vapor surface. The formation of a liquid embryo at the interface between a metastable super-saturated vapor and another solid phase is one type of heterogeneous nucleation.

As in the case of heterogeneous nucleation of vapor bubbles, the analysis of homogeneous nucleation of liquid droplets can be extended to heterogeneous nucleation at a solid-vapor interface. Because the analysis of the kinetics of the heterogeneous nucleation process is very similar to that for the comparable homogeneous nucleation process, the analysis for heterogeneous nucleation will only be briefly summarized here. If the solid surface is idealized as being perfectly smooth, in general, the shape of a droplet at the surface will be dictated by the shape of the surface itself, the interfacial tension σ, and the contact angle θ. For a flat, solid surface, the embryo liquid droplet will have a profile like that shown in Fig. 1. We will specifically consider the heterogeneous nucleation process in which formation of a droplet embryo occurs in a system held at constant temperature T_v and pressure P_v. If the embryo shape is idealized as being a portion of a sphere, it follows directly from its geometry that the embryo volume V_l and the area of the liquid-vapor (A_{lv}) and the solid-liquid interfaces (A_{sl}) are given by

$$V_l = [\pi r^3/3] (2 - 3 \cos \theta + \cos^3 \theta) \quad (1)$$

$$A_{lv} = 2 \pi r^2 (1- \cos \theta) \quad (2)$$

$$A_{sl} = \pi r^2 (1 + \cos \theta) \quad (3)$$

In the above, θ is the liquid contact angle and r is the spherical cap radius indicated in Fig. 1.

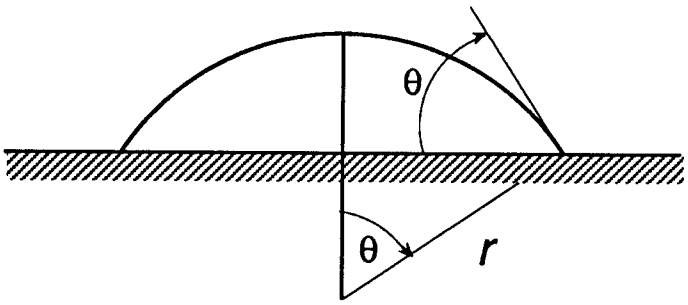

Fig. 1. An embryo liquid droplet formed at an idealized liquid-solid interface.

Using the availability function of the system approach, this function is usually associated with the maximum (reversible) work that can be extracted from the system to bring it entirely to an equilibrium reference state at T_l and P_l. It is known from basic thermodynamic considerations that equilibrium requires that the change in the total availability approach zero, and the total availability of the system (Ψ) must be a minimum for stable equilibrium. Spontaneous internal changes always result in a decrease in the availability of the system.

It follows directly from the same arguments presented for the homogeneous case that the equilibrium condition corresponds to a maximum value of the change of the availability of the system ($\Delta\Psi$) and is therefore an unstable equilibrium. As in the homogeneous case, $\Delta\Psi$ is expected to increase to a maximum and then decrease with increasing radius r. This once again leads to the conclusion that embryos having a radius less than r_e spontaneously disappear, while those having a radius greater than r_e spontaneously grow.

The determination of the kinetic limit of supersaturation of the heterogeneous nucleation is in a manner similar to that for the homogeneous nucleation case considered previously. The details are virtually identical to those of the homogeneous nucleation analysis presented, and hence they will not be presented here. There are, however, two important differences in the heterogeneous nucleation analysis. First, as an initial step in the analysis, it is postulated that, at equilibrium, the number density of embryos containing n molecules per unit of interface area N_n is given by

$$N_n = N_v^{2/3} \exp [- \Delta\Psi (r) / K T_v] \qquad (4)$$

where N_v is the number density of vapor molecules per unit volume and $\Delta\Psi(r)$ is the availability function previously defined. For the heterogeneous nucleation process considered here, only vapor molecules near the solid surface can participate in embryo droplet formation. To account for this condition, the factor multiplying the exponential term in Eq. (4) is taken to be $N_v^{2/3}$, which is representative of the number of vapor molecules immediately adjacent to the solid surface per unit of surface area.

The second different aspect of the heterogeneous analysis is the relationship between the number of molecules n in the embryo and its radius:

$$n = [N_A \pi r^3 / 3M v_l] (2 - 3 \cos\theta + \cos^3\theta) . \qquad (5)$$

This relation differs from that used in the analysis of homogeneous nucleation because the embryo geometry is different. Analysis of the kinetics of the heterogeneous nucleation process incorporates these two changes and makes use of the expansion for $\Delta\Psi$ developed for this case.

Carrying the analysis to completion yields the following relation between the rate of embryo formation J (m^{-2} s^{-1}) and the system conditions and properties:

$$J = \left(\frac{2\sigma F N_A}{\pi M}\right)^{1/2}\left(\frac{P_v}{RT_v}\right)^{5/3}\left(\frac{N_A}{M}\right)^{2/3} v_l F \left(\frac{1-\cos\theta}{2}\right)\exp\left(\frac{-16\pi(\sigma F / RT_v)^3 v_l^2 N_A}{3M\left\{\ln[P_v / P_{s\infty}]\right\}^2}\right) \quad (6)$$

where F is defined by

$$F = (2 - 3\cos\theta + \cos^3\theta) / 4 .$$

If θ is taken to be 180° and $N_v^{2/3}$ is replaced by N_v, Eq. (6) becomes identical to the expression

$$J = \left(\frac{P_v}{KT}\right)^2 \frac{M}{N_A\rho_l}\sqrt{\frac{2\sigma}{\pi m}}\exp\left(\frac{-16\pi\sigma^3}{3KT^3(\rho_l R)^2}\left(\ln\left(\frac{P_v}{P_{s\infty}}\right)\right)^{-2}\right) \quad (7)$$

where

J Nucleation rate per unit volume (m^{-2} s^{-1})
P_v Local vapor partial pressure of liquid metal
K Boltzman constant = 1.38054×10^{-23} J/molecules K
M Molecular weight
N_A Avogadro's Number = 6.03×10^{26} molecules/kg mol
ρ_l Liquid density
m Molecular mass = M/N_A
T Local vapor flow temperature
σ surface tension

obtained in the previous report for homogeneous droplet nucleation.

As in the homogeneous nucleation case, J is interpreted as the rate at which embryos of critical size are generated. As J increases, the probability that a bubble/droplet will exceed critical size and grow spontaneously becomes greater. If a threshold value of J is specified as corresponding to the onset of nucleation, the corresponding vapor temperature $T_v = (T_v)_{SSL}$ for the specified system pressure can be determined from Eq. (6). Alternatively, for the specified threshold J value, the limiting supersaturation pressure can be determined for a given system temperature.

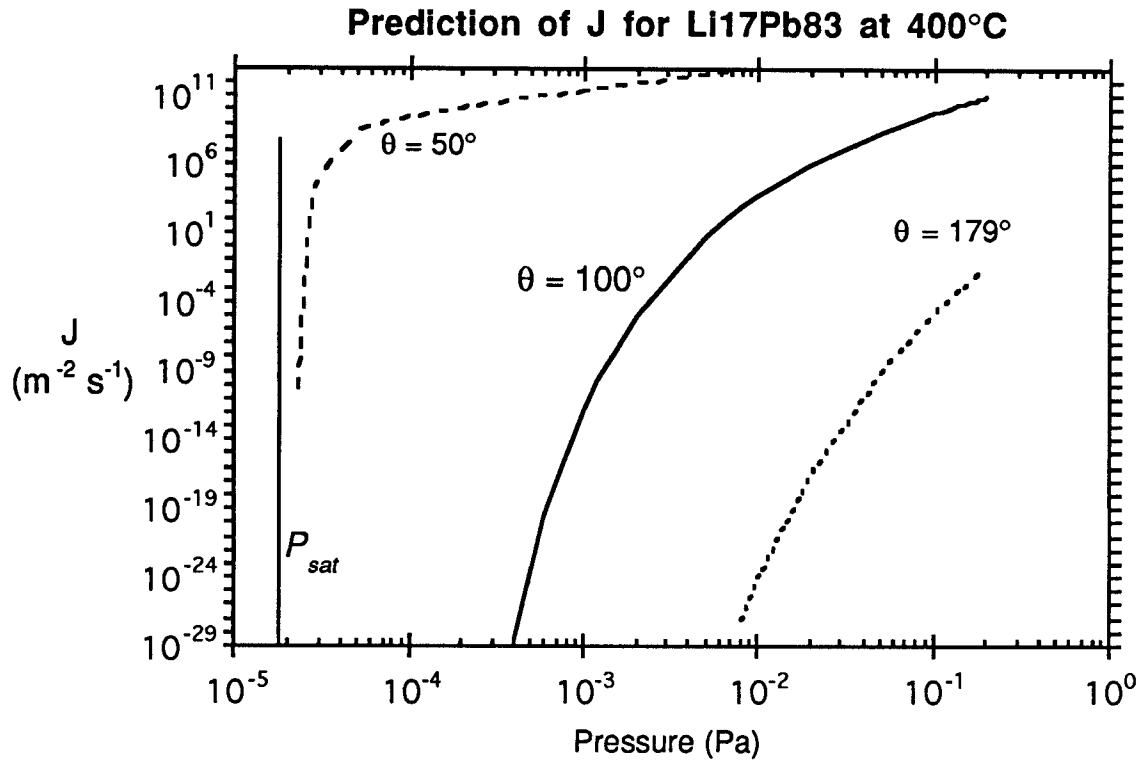

Fig. 2. Variation of the rate of embryo formation at a Li17Pb83-solid interface with vapor pressure as predicted for different contact angles by analysis of the kinetics of embryo droplet formation.

For $Li_{17}Pb_{83}$ vapor at 400°C, the variation of J with vapor pressure as predicted by Eq. (6) is shown in Fig. 2 for several values of liquid contact angle.

Assuming that a fixed threshold value of J would apply for all contact angles, it is clear that the predicted value of $(P_v)_{SSL}$ decreases with decreasing contact angle toward the normal saturation vapor pressure. At a liquid contact angle of 50° or less, the difference between the predicted $(P_v)_{SSL}$ value and $P_{sat}(T_v)$ is negligible for virtually any threshold value of J between 10^{-11} and 10^{6}.

Contact angles for virtually all real systems lie between zero and about 110°, and for metal surfaces with nonmetallic liquids, the contact angle is often below 50°. The results of the above analysis therefore suggest that condensation can be initiated at a solid surface in contact with the vapor at supersaturation levels significantly below those required for homogeneous nucleation, if the liquid phase of the vapor wets the surface reasonably well.

It is quite possible for a thin microfilm of liquid to be absorbed on all or part of a solid surface. This is particularly true for high-energy surfaces such as metals. In addition, when water is the liquid, its polar nature can enhance the tendency of water molecules to attach to portions of the solid surface. (Many oxides and corrosion-produced compounds on metal surfaces are hydrophilic.) Patches of adsorbed liquid molecules on the solid surface can thus serve as nuclei for condensation of the liquid phase when the vapor is supersaturated. Condensation on the surface

can begin as the formation of very small droplets on the surface at the sites of these nuclei. This so-called dropwise condensation process is, in fact, commonly observed when water vapor in air condenses on a cold beverage glass. This is usually interpreted as being a direct consequence of the fact that the liquid poorly wets the glass, except at nuclei locations where water molecules have adsorbed to crevices (scratches) or foreign matter (such as dust particles) on the surface. Dropwise condensation is discussed further in the next section.

V. Dropwise Condensation

Dropwise condensation may occur on a solid surface cooled below the saturation temperature of a surrounding vapor when the surface is poorly wetted except at locations where well-wetted contaminant nuclei exist. The poorly wetted surface condition can result from contamination or coating of the surface with a substance that is poorly wetted by the liquid phase of the surrounding vapor. In practice, this can be achieved for liquid metal condensation by permanently coating the surface with a low surface-energy polymer or a noble metal. This method of promoting dropwise condensation is of particular interest because it holds the prospect of providing continuous dropwise condensation. Dropwise condensation is generally the preferred mode of condensation because the resulting heat transfer coefficient may be as much as an order of magnitude higher than that for film condensation under comparable circumstances. Recent studies by Westwater and co-workers [1,2] have demonstrated that dropwise condensation of steam can be consistently obtained on gold and silver surfaces. The occurrence of dropwise condensation on gold and silver surfaces would appear to contradict the reasoning that high-surface-energy metal surfaces should be well wetted by the liquid phase, producing film condensation instead of dropwise condensation. During dropwise condensation, the condensate is usually observed to appear in the form of droplets, which grow on the surface and coalesce with adjacent droplets. When droplets become large enough, they are generally removed from the surface by the action of gravity or drag forces resulting from the motion of the surrounding gas. As the drops roll or fall from the surface, they merge with droplets in their path, effectively sweeping the surface clean of droplets. Droplets then begin to grow anew on the freshly exposed solid surface. This sweeping and renewal of the droplet growth process is responsible for the high heat transfer coefficients associated with dropwise condensation. Despite numerous studies of dropwise condensation over the years, its mechanism remains the subject of debate. Two different types of models have been proposed. The first model type is based on the premise that droplet formation is a heterogeneous nucleation process like that described in Section IV. Droplet embryos are postulated to form and grow at nucleation sites, while portions of the surface between the growing droplets remain dry. Experimental evidence supporting this physical model of the condensation process has emerged from several experimental investigations. A model of the dropwise condensation process that includes droplet nucleation, growth, removal, and renucleation on reexposed sites was developed by Gose et al. [3]. In the second type of dropwise condensation model, it is postulated that condensation occurs initially in a filmwise manner, forming an extremely thin film on the solid surface. As condensation continues, this film eventually reaches a critical thickness, estimated to be about 1 μm, at which point it ruptures and droplets form. Condensation then continues on the surface between the droplets that form when the film ruptures. Condensate produced in these regions is drawn to adjacent drops by surface tension effects. Droplets also grow by direct condensation on the droplet surfaces themselves. The results of several investigations seem to support this type of interpretation of the condensation process. These results indicate that condensation occurs entirely between droplets on a very thin liquid film. In contrast, it is postulated in the first model described above that condensation occurs only on the droplets, and not on the surface between them. The rate of condensation on the larger droplets is less than

on the smaller ones because of the higher resistance to heat conduction through larger drops. The large drops therefore grow primarily through coalescence. This model implies that most of the heat transfer during dropwise condensation is transferred to that portion of the surface covered with the smallest droplets. Detailed modeling of dropwise condensation heat transfer based on the first model hypothesis has, in fact, been attempted by several investigators. These models generally idealize the heat transfer process. Correlations for the heat transfer coefficient associated with dropwise condensation have been proposed by a number of investigators. One example is the following correlation, proposed by Peterson and Westwater [4] for dropwise condensation of steam and ethylene glycol:

$$Nu = 1.46 \times 10^{-6} (\mathrm{Re}^*)^{-1.63} \Pi_k^{1.16} \mathrm{Pr}_l^{0.5}$$

where

$$Nu = \frac{2h\sigma T_{sat}}{\rho_l h_{lv} k_l (T_{sat} - T_w)}$$

$$\mathrm{Re}^* = \frac{k_l (T_{sat} - T_w)}{\mu_l h_{lv}}$$

$$\Pi_k = -\frac{2\sigma T_{sat}}{\mu_l^2 h_{lv}} .$$

While correlations of this type can be made to agree quite well with data for a specific surface and fluid combination their general applicability has not been demonstrated. The use of such a correlation for circumstances other than those for which it was developed is questionable at best. Further discussion of correlation for dropwise condensation is provided in the review article by Merte [5].

References

1. Woodruff, D. M. and Westwater, J. W., "Steam condensation on various gold surfaces," *J. Heat Transfer*, vol. 103, 685-692, 1981.
2. O'Neil, G. A., and Westwater, J. W., "Dropwise condensation of steam on electroplated silver surfaces," *Int. J. Heat Mass Transfer*, vol. 27, pp. 1539-1549, 1984.
3. Gose, E., Mucciordi, A. N., and Bear, E., "Model for dropwise condensation on randomly distributed sites," *Int. J. Heat Mass Transfer*, vol. 10, pp. 15-22, 1967.
4. Peterson, A. C., and Westwater, J. W., "Dropwise condensation of ethylene glycol," *Chem. Eng. Prog. Symp. Ser.*, vol. 62, no. 64, pp. 135-142, 1966.
5. Merte, H., Condensation heat transfer," *Adv. Heat Transfer*, vol. 9, pp. 181-272, 1973.